catalysts

MDPI

Article

(002) Oriented $Bi_2O_2CO_3$ Nanosheets with Enhanced Photocatalytic Performance for Toluene Removal in Air

Junping Ding [1,2], Huanchun Wang [3], Yidong Luo [1], Yushuai Xu [1], Jinsheng Liu [2] and Yuanhua Lin [1,*]

1 State Key Laboratory of New Ceramics and Fine Processing, School of Materials Science and Engineering, Tsinghua University, Beijing 100084, China; djp15@mails.tsinghua.edu.cn (J.D.); ydluozd@163.com (Y.L.); xuyushuai5736@163.com (Y.X.)
2 China Astronaut Research and Training Center, Beijing 100094, China; goldsix@sohu.com
3 High-Tech Institute of Xi'an, Xi'an 710025, Shanxi, China; wang-hc12@tsinghua.org.cn
* Correspondence: linyh@mail.tsinghua.edu.cn; Tel.: +86-10-6277-3741

Received: 23 February 2020; Accepted: 26 March 2020; Published: 2 April 2020

Abstract: Layer-structured $Bi_2O_2CO_3$ is a novel photocatalyst for eliminating environmental pollutants. In this work, $Bi_2O_2CO_3$ nanosheets were synthesized by hydrothermal methods, followed by annealing in nitrogen. (002) oriented $Bi_2O_2CO_3$ nanosheets were obtained and characterized by XRD, SEM, XPS, BET and UV-Vis diffuse reflectance spectra. Photocatalytic properties were investigated by toluene removal in air, with the assistant of $Bi_2O_2CO_3$ nanosheets under artificial irradiation. Our results show that $Bi_2O_2CO_3$ annealed in nitrogen exhibited high full-light-driven photocatalytic activity for toluene photocatalytic decomposition, which may be ascribed to facet orientation evolution during the annealing process and enhanced efficient charge separation. The sample annealed at 150 °C for 8 h (BOC-150-8 h) showed high stability and the highest toluene removal rate, which was up to 99%. The final degradation products were detected by gas chromatography–mass spectrometer (GC-MS) and CO_2 was verified to be the primary product. Photocatalytic mineralization of toluene in air over $Bi_2O_2CO_3$ was proposed. This work may provide a foundation for application of annealed $Bi_2O_2CO_3$ in indoor air purification.

Keywords: $Bi_2O_2CO_3$; toluene decomposition; crystal orientation; volatile organic compound (VOCs); photocatalysis

1. Introduction

Volatile organic compounds (VOCs) are one of the major indoor pollutants which derive from sources including paints, varnishes, solvents, furniture, etc. Benzene and its derivatives such as toluene, xylenes are typical representative substances of VOCs. Toluene exposure may cause indisposed symptoms of lethargy, dizziness and confusion. Toluene is considered as a strong carcinogen which is heavily restricted by National Ambient Air Quality Standard [1–4]. The removal of benzene and its derivatives in air is a huge challenge for environmental restoration. Technologies such as physicochemical adsorption, gas separation, biodegradation and chemical degradation are investigated for indoor air purification. Among all the above-mentioned techniques, semiconductor photocatalysis, which is an advanced oxidation process based on oxidation-reduction reaction, demonstrated great prospect due to its green, sustainable and low-cost features. Variety of photocatalysts have been studied, including oxides, sulfide, nitride, phosphide, novel composites and delicate micro-nano structures. TiO_2 is one of the earlier photocatalysts for air purification. Though TiO_2 showed primordial activity for air pollution control, photocatalysis by semiconducting materials loaded with non-metal or noble

metals is an excellent strategy for removal of gaseous toluene. By coupling atomic-scale Pt with MoS_2 as co-catalysts, TiO_2 showed superior performance than pure one [5]. Several TiO_2 based composites and non-TiO_2-based photocatalysts, such as ZnO, Fe_2O_3, g-C_3N_4, were reported for photocatalytic oxidation of VOCs and inorganic pollutants [6–11].

More recently, a variety of bismuth-containing compounds have been studied as emerging photocatalysts, such as Bi_2O_3, Bi_2WO_4, $Bi_2O_2CO_3$, BiOX (X = Cl, Br, I), etc. [12–17]. A total removal efficiency of 76.3% was achieved by BiOI/Bi_2WO_6/ACF composite photocatalysts for 500 mg/m^3 toluene [18]. $Bi_2O_2CO_3$, was used to photocatalytic removal of NO; introducing oxygen vacancies can significantly enhance the performance. The photocatalytic removal ratio of NO was increased significantly from 10% for pure BOC to 50.2% for OV-BOC because of the multiple roles played by the oxygen vacancies [19].

$Bi_2O_2CO_3$ is ascribed to the aurivillius structure and layered with alternative stacking $(Bi_2O_2)^{2+}$ sheets interleaved by CO_3^{2-} groups in crystal structure [20–22]. These years, its application in photocatalysis has been explored. A variety of attempts have been investigated to enhance the photocatalytic performance of $Bi_2O_2CO_3$, such as: doping [23], heterojunctions construction with smaller band gap semiconductors and morphology controlling with especial crystal facets exposed [24,25]. The exposed {001} facets of $Bi_2O_2CO_3$ are considered to contribute much more photocatalytic activity because the Bi-O square anti-prism with 8-coordination compressed along the c-axis supply lots of oxygen defects which more preferred to generate the electron and vacancy [26,27]. Although $Bi_2O_2CO_3$ has been studied extensively, the research and application of photocatalysis now mainly focuses on photolysis of removal NO_X [28,29], water to generate hydrogen [30] and degradation of organic pollutants in water such as methyl orange (MO), rhodamine B (RhB), methylene blue (MB) and their mixed solutions [31]. The application of photocatalysis on removal toluene in air is limitedly reported [32].

Herein, we report a facile hydrothermal method to fabricate $Bi_2O_2CO_3$ nanosheets with (002) facet exposed, followed by annealed in nitrogen. $Bi_2O_2CO_3$ samples annealed at diffident temperature for various times and their photocatalytic properties for removal toluene in air under the artificial irradiation are investigated comparatively. Based on the close correlation between the structure characteristics and physicochemical properties of the material, $Bi_2O_2CO_3$ annealed at 150 °C for 8 h has proved to be most active, with removal rate up 99%. Permineralization of toluene in photocatalysis is proposed based on the characterization; CO_2 was verified to be the primary product. This work may probably extend to application of $Bi_2O_2CO_3$ in air purification.

2. Results and Discussion

2.1. $Bi_2O_2CO_3$ Annealed in Nitrogen at Different Temperature

2.1.1. Characterization

As shown in Figure 1, the sample fabricated by hydrothermal method was indexed as tetragonal $Bi_2O_2CO_3$ without impurity. Temperature had significant influence on the phase transformation during anneal in nitrogen. When BOC annealed at 150 °C for 4 h (BOC-150-4 h), the diffracted intensity of (002) peak was stronger than primitive BOC. The diffracted intensity ratios of (002)/(013) and (004)/(013) were 0.25 and 0.15 for primitive BOC. The ratios were 0.60 and 0.28 for BOC-150-4 h, much larger than that for primitive BOC. That indicated tetragonal $Bi_2O_2CO_3$ went crystal facets evolution during annealing under 150 °C for 4 h. (002) facet was superior at high temperature [33–36]. Nevertheless, higher temperature led to phase transition from BOC to Bi_2O_3, as revealed by XRD results. The sample of BOC-350-4 h had diffracted peaks located at 27.38°, which could be indexed as the (012) facet of Bi_2O_3. BOC-450-4 h could be indexed to α-Bi_2O_3, according to XRD patterns. BOC was reported to be unstable at high temperature. When heated at 350 °C, BOC decomposed and transformed to Bi_2O_3 and CO_2 [37]. A moderate temperature was proposed for BOC annealing. The sample ofBOC-250-4 h

showed no phase transition, however, the diffracted peaks ratio of (002)/(013) and (004)/(013) were 0.46 and 0.25, those were smaller than that of BOC-150-4 h.

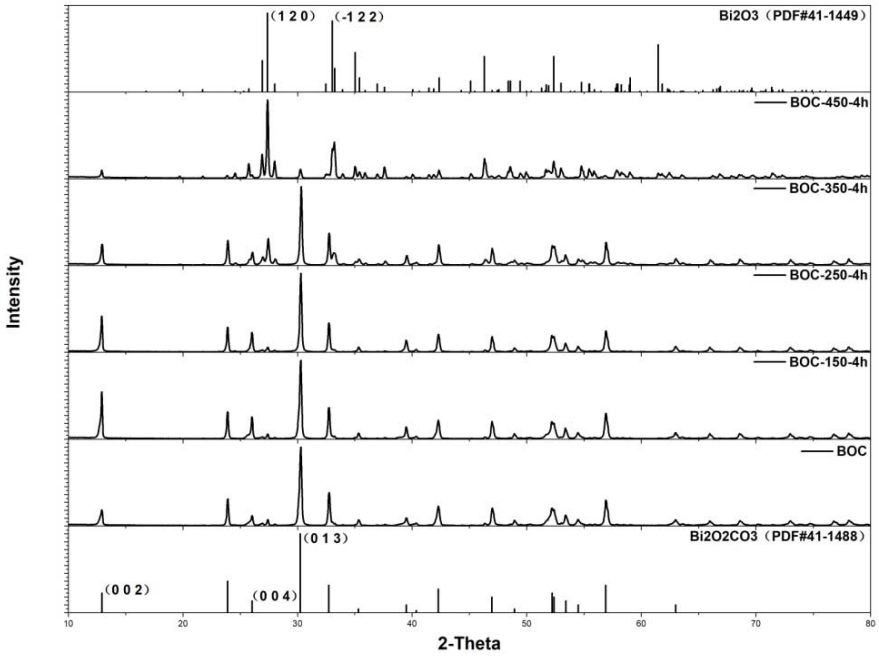

Figure 1. Patterns of as-prepared samples at different temperature.

2.1.2. Photocatalytic Activity

In the present work, the photocatalytic performance of BOC annealed in nitrogen was investigated by removal toluene in air. The results of removal toluene by BOC annealed in N_2 at different temperature for 4 h are shown in Figure 2 and Figure S2. The rate of photocatalytic degradation follows a pseudo first order kinetics based on the Langmuir–Hinshelwood model:

$$\ln(C_0/C_t) = kt \quad (1)$$

where C_0 is the equilibrium concentration, C_t is the concentration at any time, k is the first-order rate constant and t is the photocatalytic time. According to Formula (1), the k values for BOC, BOC-150-4 h, BOC-250-4 h, BOC-350-4 h, BOC-450-4 h are 0.0100, 0.0105, 0.0031, 0.0016 and 0.0013 min^{-1}, respectively, from which we could observe that the photo degradation rate constant of BOC-150-4 h is larger than any others. BOC and BOC-150-4 h showed almost the same impressive performance over toluene removal. BOC-250-4 h had a slightly worse performance than BOC-150-4 h and raw BOC nanosheets. Samples BOC-350-4 h and BOC-450-4 h showed negligible effectiveness for toluene removal. The content of toluene after photocatalysis in chamber showed no macroscopic different compared with that of controlled experiment. Photocatalysis test's results revealed that $Bi_2O_2CO_3$—eitheruntreated BOC or annealed at low temperature—had remarkable ability in toluene removal. However, Bi_2O_3 showed suppressive effect.

{001} exposing facets over $Bi_2O_2CO_3$ have been reported to show photocatalytic activity due to efficient separation and migration of photoinduced electron-hole pairs [16]. Meanwhile, β-Bi_2O_3 nanosheets exposed with active {001} facets prepared through annealing $Bi_2O_2CO_3$ have shown improved photocatalytic oxidation of NO [24]. However, the underlying mechanisms are still not fully understood.

In this work, exposing facets of $Bi_2O_2CO_3$ crystals appeared to have relevant effect on photocatalytic activity. BOC-150-4 h had the strongest diffracted intensity of (002) peak, along with almost the best photocatalytic activity.

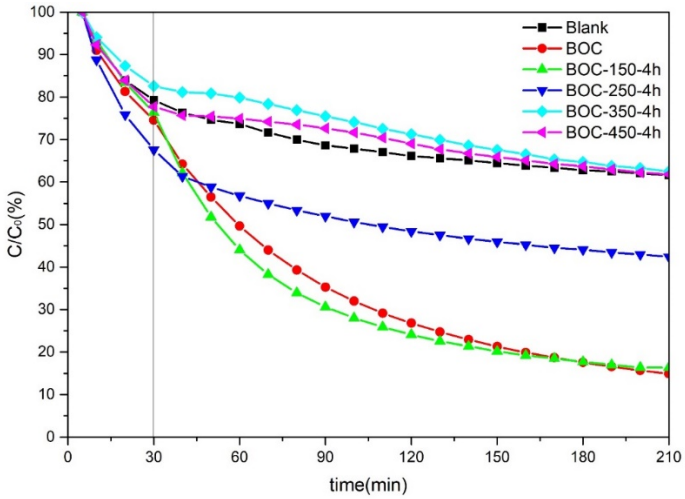

Figure 2. Efficiencies of removal toluene by BOC annealed in nitrogen at different temperature.

2.2. $Bi_2O_2CO_3$ Annealed in Nitrogen for Various Time at 150 °C

2.2.1. Morphology and Structural Properties

To further understand the effects of annealing time and exposing facets to photocatalytic activity, BOC was annealed at 150 °C for various times. Powder X-ray diffraction (Figure 3) revealed that all diffraction peaks can be well indexed to the pure phase of $Bi_2O_2CO_3$, without impurity peaks appearing in all as-prepared samples. This suggests that annealing $Bi_2O_2CO_3$ in nitrogen at 150 °C had not led to phase transformation. Nevertheless, the evolution of crystal facets was revealed by elaborately evaluating the diffracted intensity of special peaks.

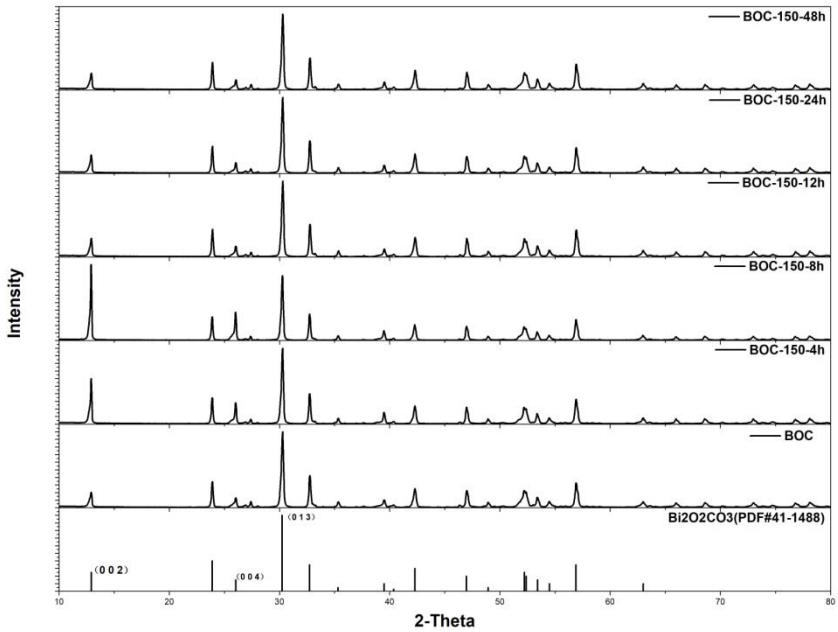

Figure 3. Patterns of as-prepared samples for various times at 150 °C.

Compared to hydrothermal fabricated $Bi_2O_2CO_3$, (002) facet exposed dominantly after BOC were annealed for 4 h and 8 h at 150 °C. The diffracted intensity ratio of (002)/(013) of BOC-150-4 h and BOC-150-8 h were 0.60 and 1.17, that was much larger than 0.25 of primitive BOC (JCPDS 41-1488). The ratio of BOC-150-8 h has been increased by 92%. Prolonging the annealing time further to 12 h, 24 h or 48 h, unexpectedly, the enhanced diffracted intensity ratio of (002)/(013)restored to the value of BOC.

On the basis of the above analyses, it could be speculated that during annealing, hydrothermal fabricated $Bi_2O_2CO_3$ nanosheets underwent a delicate evolution process of dominantly exposed facets.

In the following, the surface composition of the annealing BOC was further investigated by XPS technique. Figure 4 presents the detection results of the high-resolution XPS spectra. As shown in Figure 4a, the relative peaks of the C-1s, O-1s and Bi-4f elements have been successfully detected. Therein, the C-1s peak at a binding energy of 284.8 eV can be attributed to adventitious hydrocarbon; the peak observed at 289.0 eV should be ascribed to the carbon of C–O bond in $Bi_2O_2CO_3$ (Shown in Figure 4b) [38]. The O-1s binding energy of 530.3 eV in Figure 4c can be attributed to the lattice oxygen inthe $(Bi_2O_2)^{2+}$ layers of $Bi_2O_2CO_3$ [39]. In Figure 4d–f, the two apparent characteristic peaks for Bi-4f located at 159.1 and 164.5 eV are attributed to Bi-4$f_{7/2}$ and Bi-4$f_{5/2}$ in $Bi_2O_2CO_3$, which indicating the existence of Bi^{3+} in the sample [40,41].

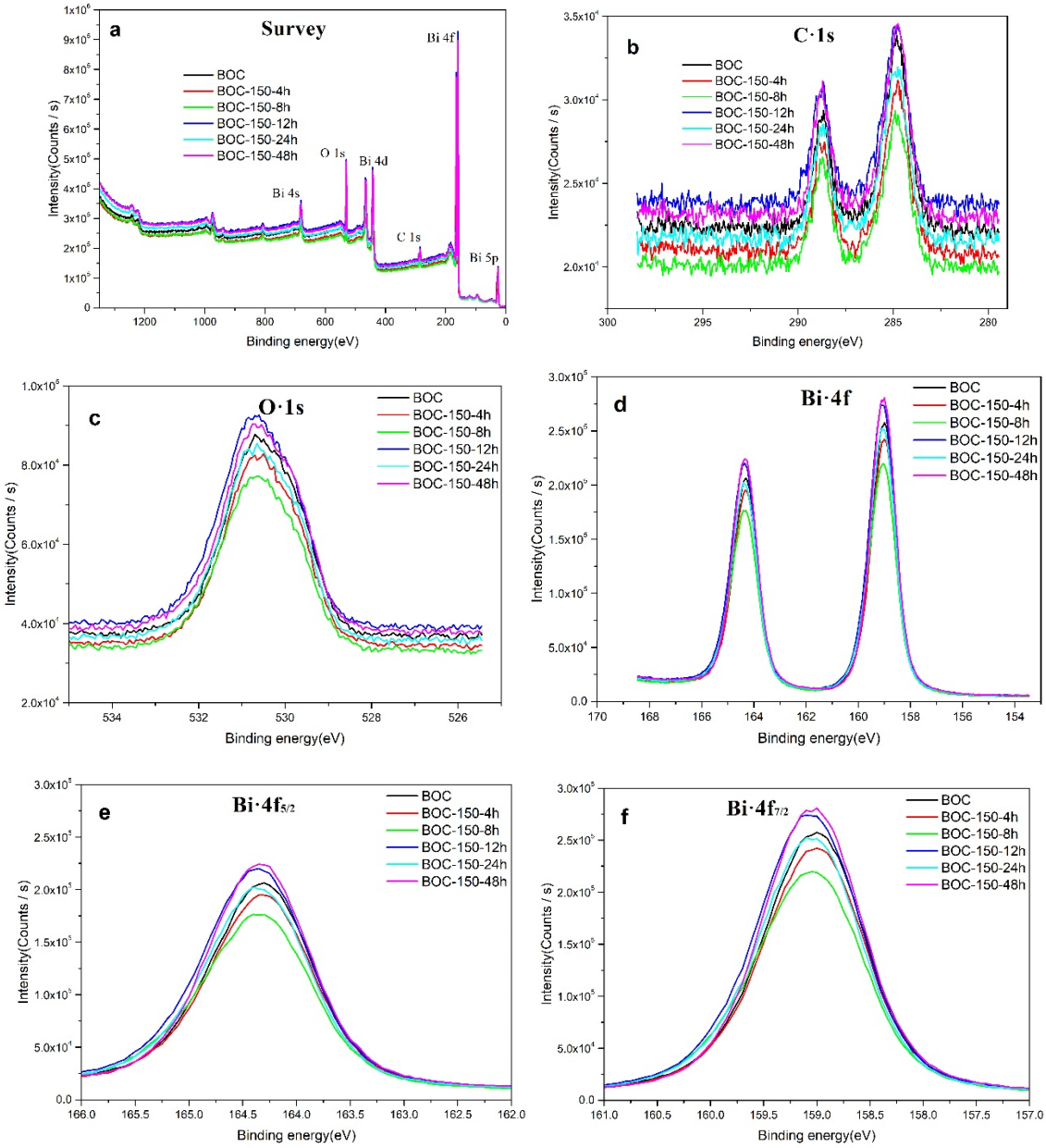

Figure 4. Spectra of BOC samples: survey scan (**a**), C1s (**b**), O1s (**c**) and Bi4f (**d**–**f**).

SEM images were obtained to investigate the morphology of the samples, which are presented in Figure 5. According to the SEM images, samples prepared by hydrothermal method showed irregular

polyhedral structures with lateral length of 300~900 nm (Figure 5a). After annealing at 150 °C for various times, the appearance of BOC showed negligible changes compared to the primary sample (Figure 5b, Figure S3). The typical thickness of the annealed sample was few tens of nanometers. It appeared to be two-dimensional nanosheets [42]. It implied that a low temperature annealing process had no apparent effects on the morphologies. This was further supported by BET measurement.

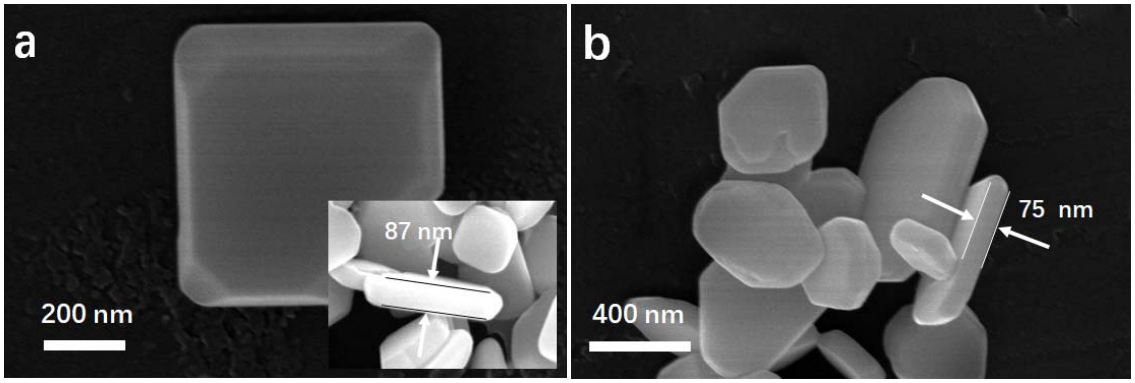

Figure 5. SEM images of BOC (**a**) and BOC-150-8 h (**b**).

The BET surface area test results of as-prepared samples are shown in Table 1. It was found that the specific surface area and pore volume of the sample BOC-150-8 h were 3.556 m^2/g and 0.5319 cm^3/g, respectively, which was much larger than the others. Moreover, the pore volume of all BOC was much larger than most of other bismuth oxides and the different morphology of $Bi_2O_2CO_3$ materials. The specific surface area of BOC-150-8 h is similar to plate-like $Bi_2O_2CO_3$ (Shown in Tables S1 and S2) [43].Therefore, the larger BET surface area of BOC-150-8 h may result in better catalysis performance by providing more actives sites than the other samples.

Table 1. Specific surface area of BOC-annealing in N_2 for various times at 150 °C.

	BOC	BOC-150-4 h	BOC-150-8 h	BOC-150-12 h	BOC-150-24 h	BOC-150-48 h
Surface area (m^2/g)	1.335	1.354	3.556	2.687	1.311	0.812
Pore volume (cm^3/g)	0.3251	0.3361	0.5319	0.3542	0.3171	0.2178

2.2.2. Band Structure Analysis

The UV-Vis diffuse reflectance spectra of the samples were examined, and the results presented in Figure 6. It can be seen that the bandgap of all the samples can be decided about 2.8 eV.

The conduction band (CB) and valence band (VB) potentials of as-prepared samples were calculated using the following empirical formulae [44]:

$$E_{VB} = X - E^e + 0.5E_g \quad (2)$$

$$E_{CB} = E_{VB} - E_g \quad (3)$$

where E_{VB} and E_{CB} are the semiconductor VB and CB potentials, respectively, X is the absolute electronegativity of the semiconductor, E^e is the energy of free electrons on the hydrogen scale (~4.5 eV), E_g is the semiconductor band gap. Whereas the absolute electronegativity is the energy difference between the vacuum level and the mid-gap position of semiconductor, the work function value is the difference between the vacuum level and the Fermi energies, which of pure $Bi_2O_2CO_3$ is zero [26]. According to the above formulae, the E_{VB} and E_{CB} of the samples were calculated, and the band gap

structures were obtained (Figure 7). It can be concluded that valence band edge position and conduction band edge position become more negative when we prolonged the annealing time in nitrogen.

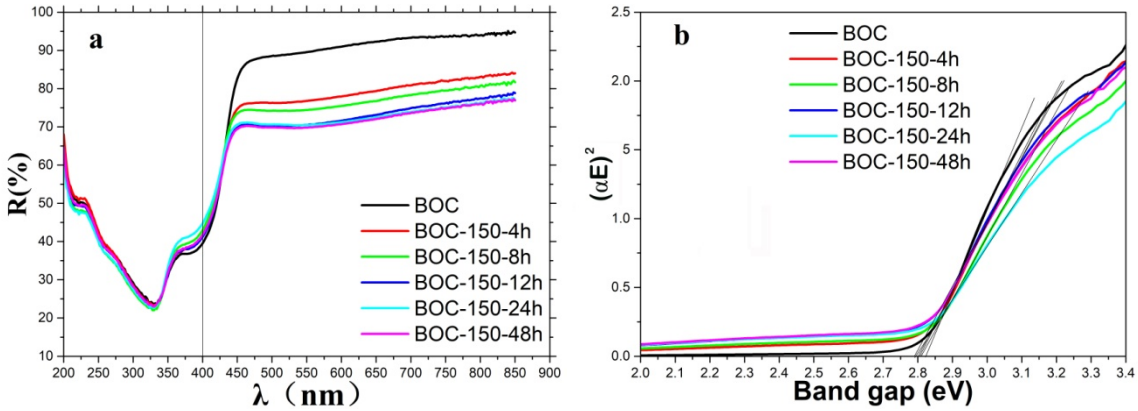

Figure 6. UV-Vis diffuse reflectance spectra of as-prepared samples (**a**) and band gap fitting with K-M relation (**b**).

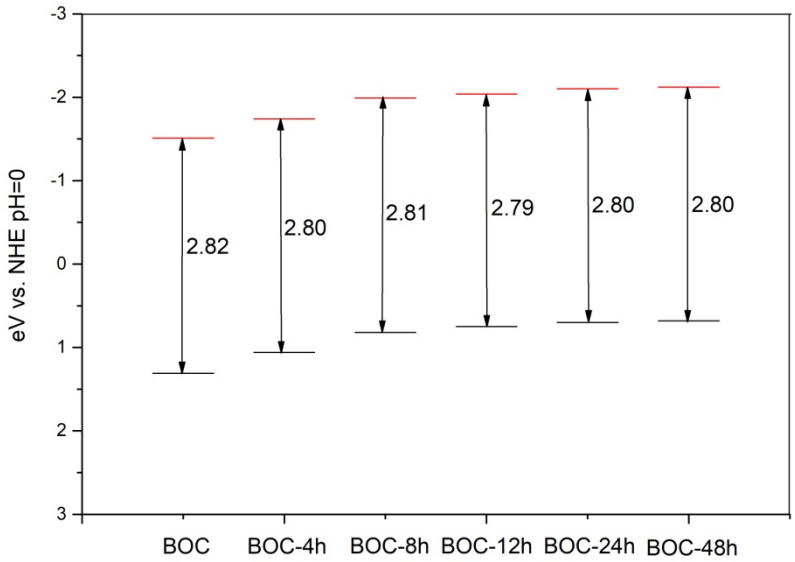

Figure 7. Band structure of as-prepared BOC (E_{CB}, redand E_{VB}, black).

2.2.3. Photocatalytic Activity

The photocatalytic performance of annealed BOC in nitrogen for various time at 150 °C are presented in Figure 8; the digital images after reaction are shown in Figure S4. All the as-prepared BOC samples showed almost the same impressive performance for toluene removal. BOC-150-8 h was superior to any other samples, with removal rate of up to 99%. BOC-150-12 h and BOC-150-24 had a slightly worse performance, but they were better than BOC-150-4 h and BOC-150-48. BOC-150-48 was analogous with the raw BOC nanosheets.

On the basis of Formula (1), k values for various samples were calculated. The specific numbers for BOC-150-4 h, BOC-150-8 h, BOC-150-12 h, BOC-150-24 h, BOC-150-48 h were 0.0105, 0.0211, 0.0161, 0.0168 and 0.0116 min^{-1}, respectively. BOC-150-8 h had the largest k value, with higher ratio of (002) and (004) crystal face exposed from Figure 3, which may have contributed to the separate of photo-excited hole-electron pairs that led to the photodegradation rate constant of BOC-150-8 h being larger than any others. At the same time, BOC-150-48 h had a lower reaction rate than samples heated for 4 h, 8 h, 12 h or 24 h, which suggests longer annealing times may not always result in better performance.

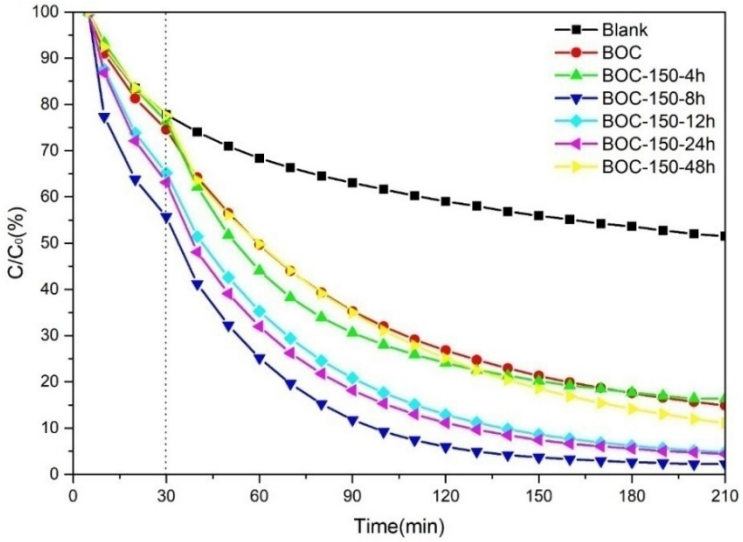

Figure 8. Photocatalytic efficiencies of removal toluene by BOC annealed in nitrogen for various time at 150 °C.

Fourier transform infrared (FTIR) spectroscopic analysis was performed for BOC-150-12 h and BOC-150-24 h; the results are shown in Figure 9. All the peaks around 694, 846, 1068 and 1390 nm may be checked to be CO_3^{2-}. The peak 553 nm is the bond Bi-O, indicating that it was $Bi_2O_2CO_3$ [45,46]. It can be believed that the decrease of toluene's concentration during the photocatalysis process was caused by degradation and no obvious reactant absorbed after reaction.

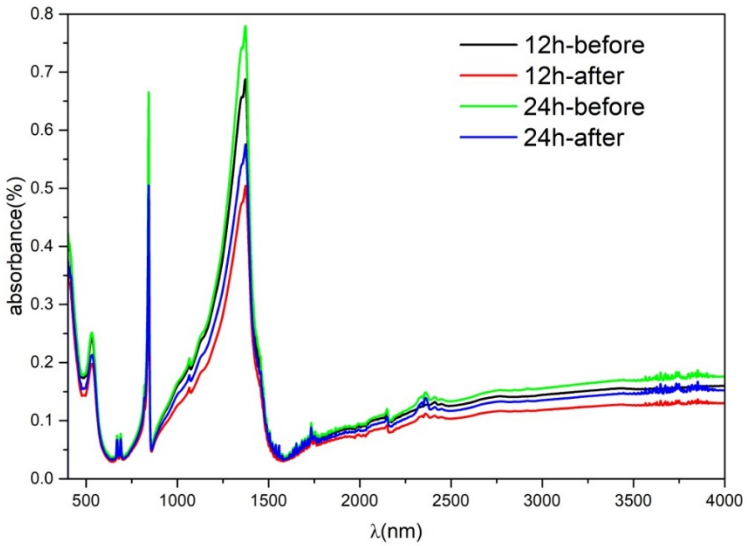

Figure 9. Spectra of the BOC-150-12 h and BOC-150-24 h samples before and after removal toluene.

The constituent and the content of the mixture in the chamber at end of photocatalysis process were measured by GC-MS; the results are shown in Table 2, Table S3, Figure 10 and Figures S5–S9. It was found that CO_2 is one of the main products of removal toluene by $Bi_2O_2CO_3$ in photocatalytic degradation. Moreover, it was presumed that the other main product is H_2O. However, little amount of benzene could be detected in the mixtures of BOC-150-4 h and BOC-150-48 h, which indicates that the benzene may have acted as one of the intermediate products during reaction. For BOC-150-48 h, the rate and quantum field of the photocatalytic CO_2 production were 19.06 umol/g and 6.67 umol, respectively, which were larger than the other samples. Furthermore, the quantum field was close to seven times of the initial quantity 1 umol, which corresponds with the mass balance of carbon.

Table 2. Constituents and content of the final products of removal toluene (%V/V).

Retention Time (min)	BOC-150-4 h	BOC-150-8 h	BOC-150-12 h	BOC-150-24 h	BOC-150-48 h
CO_2 (11.879)	95.02	98.55	99.95	99.63	94.27
Benzene (17.103)	0.12	-	-	-	0.22
Toluene (21.119)	4.86	1.45	0.05	0.37	5.51

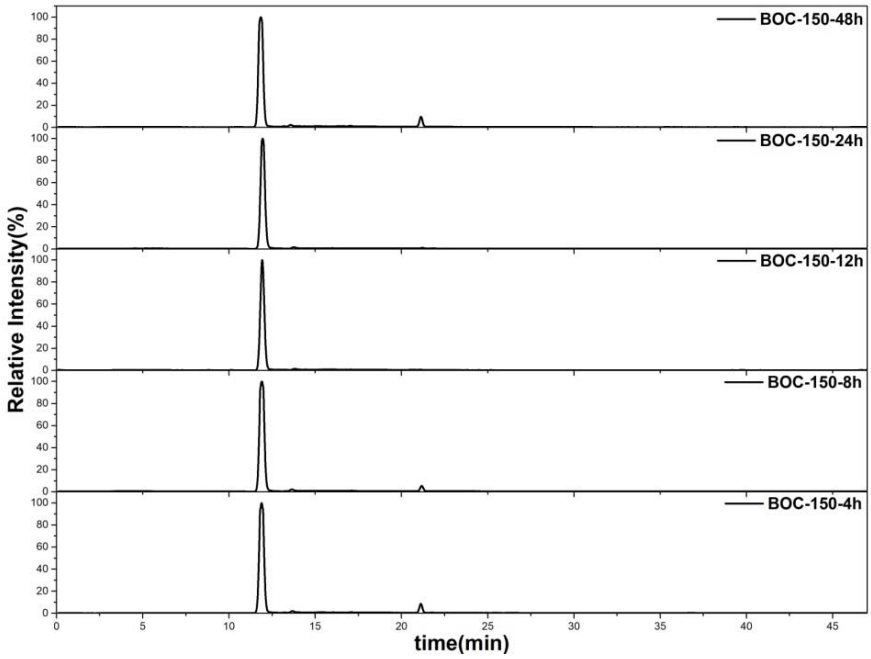

Figure 10. Total ion chromatograms of as-prepared samples.

The (002) plane belongs to {001} facets in $Bi_2O_2CO_3$ nanosheets with a high oxygen atoms density, which can lead to great catalytic activity [17]. The exposed crystal plane of (002) in $Bi_2O_2CO_3$ can not only result in higher surface area, but also help with the separation of photo excited carriers, as it leads to enhanced photocatalytic performance for toluene removal in air [25,47].

Above all, the mechanism of photocatalytic degradation of toluene is summarized in Figure 11. First of all, electrons in $Bi_2O_2CO_3$ nanosheets can be excited from valence bond to conduction bond under the irradiation of light, forming photogenerated electron-hole pairs. Second, the electrons migrate to the surface of $Bi_2O_2CO_3$, so that the surface-adsorbed O_2 is reduced to highly active species $\bullet O_2^-$. Thus, highly active $\bullet O_2^-$ oxidizes toluene to CO_2, H_2O and other intermediate products such as benzene, benzoic acid, benzaldehyde and benzyl alcohol [48]. Then h^+ oxidizes the surface-adsorbed H_2O to highly active species •OH, the active species ($\bullet O_2^-$ and •OH) oxidizes the adsorbed intermediates to CO_2 and H_2O, forming the final products CO_2 and H_2O consequently.The supposed reaction steps have listed as follows.

$$Bi_2O_2CO_3 + hv \rightarrow Bi_2O_2CO_3\ (h^+) + Bi_2O_2CO_3(e^-) \quad (4)$$

$$Bi_2O_2CO\ (e^-) + O_2 \rightarrow \bullet O_2 \quad (5)$$

$$\bullet O_2^- + C_7H_8 \rightarrow \text{intermediates} + CO_2 + H_2O \quad (6)$$

$$\bullet O_2^- + \text{intermediates} \rightarrow CO_2 + H_2O \quad (7)$$

$$h^+ + C_7H_8/\text{intermediates} \rightarrow CO_2 + H_2O \quad (8)$$

$$H_2O + h^+ \rightarrow \bullet OH + H^+ \quad (9)$$

$$\bullet OH^- + C_7H_8/\text{intermediates} \rightarrow CO_2 + H_2O \quad (10)$$

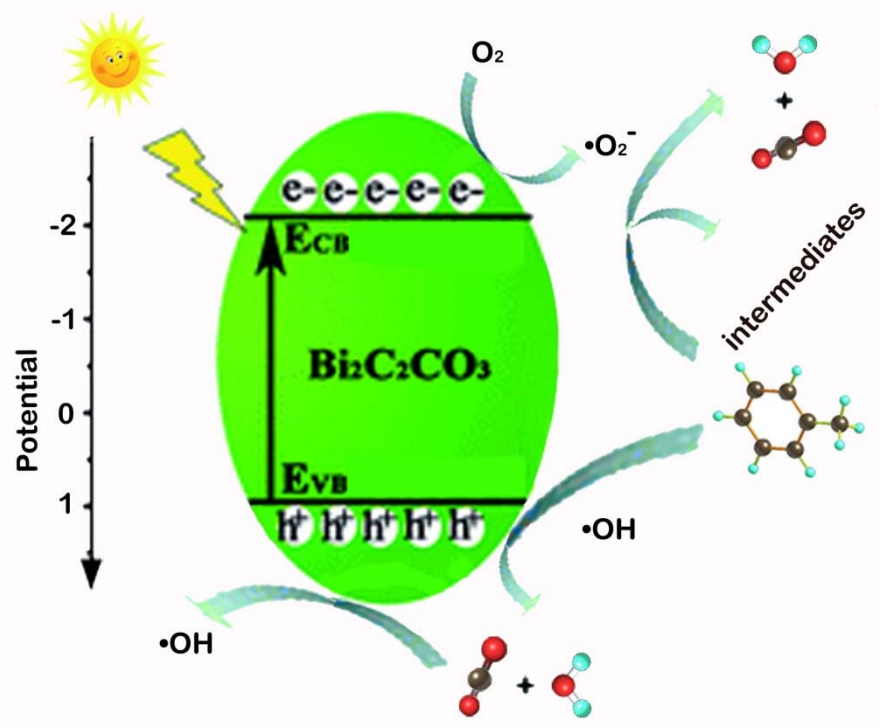

Figure 11. Photocatalytic mechanism of toluene removal by $Bi_2O_2CO_3$ nanosheets.

3. Materials and Methods

3.1. Preparation of $Bi_2O_2CO_3$ Nanosheets

All the chemical reagents used in this work were analytical-grade reagents and used without any further purification. In a typical synthesis procedure, 3 g urea (≥99.0%, Beijing Modern Orient Fine Chemistry Co. Ltd., Beijing, China) and 4.65 g Bi_2O_3 (99.99%, Aladdin Industrial Corporation, Shanghai, China) were added to 60 mL deionized water with magnetic stirring. Then the reaction mixtures were sealed in a Teflon-lined stainless-steel autoclave and heated at the temperature 180 °C under autogenous pressure for 12 h. After natural cooling to room temperature, the product was filtered, washed with deionized water and ethyl alcohol and dried at 70 °C in an oven. The specimen was labeled as BOC [42].

3.2. Preparation of $Bi_2O_2CO_3$ Nanosheets with (002) Facet Exposed

$Bi_2O_2CO_3$ nanosheets with (002) facet exposed were prepared by annealed BOC in nitrogen. For example, 2 g BOC was sealed in tube furnace (OTF-1200, Hefei Kejing Materials Technology Co. Ltd., Hefei, China) and treated at 150 °C for 4 h in nitrogen. The nitrogen flow rate was 1.2 L/min. The sample is labeled as BOC-150-4 h. BOC annealed at 250, 350 and 450 °C were labeled asBOC-250-4 h, BOC-350-4 h, BOC-450-4 h.

For comparison, BOC was also treated at 150 °C for 8 h, 12 h, 24 h, 48 h. The final samples labeled as BOC-150-8 h, BOC-150-12 h, BOC-150-24 h, BOC-150-48 h [37].

3.3. Characterization and Photocatalysis Test

The Powder X-ray diffraction (XRD) patterns were obtained from a diffractometer (D8-Advance, Bruker, Karlsruhe, Germany) using monochromatized Cu Kα (λ = 1.54056 nm) radiation with scanning speed of 0.15°/s. The morphology of the samples was observed by a field emission scanning electron microscope (JSM-7001F, JEOL, Tokyo, Japan) operating at a 5 kV. UV-Vis-NIR diffuser reflectances (DRS) were carried out on a UV-Vis-NIR spectrometer (Lambda 950, PerkinElmer, Cambridge, MA, USA). The XPS spectra measurements were conducted on a X-ray photoelectron spectroscopy (ESCALAB

250Xi, Thermo Fisher, San Jose, CA, USA). The specific surface area was measured on an automated gas sorption analyzer (AutosorbiQ2, Quantachrome, Boynton Beach, FL, USA). Ultraviolet photoelectron spectroscopy (UPS) was carried out on the ultraviolet photoelectron spectrometer (AC-2, RIKEN KEIKI, Osaka, Japan). The Fourier transform infrared (FTIR) spectra was got by the Fourier transform infrared (FTIR) spectrometer (Nicolet iS50, Thermo Fisher, Waltham, MA, USA).

The photocatalytic properties of the specimen were evaluated by removal toluene in air with the assistant of photocatalyst in a home-made photocatalysis equipment (Figure S1). Before the photocatalytic test, the inter space of the unit was first substituted with nitrogen to expel the oxygen and moisture. Toluene was supplied by toluene standard gas with concentration of 50.1 ppm balanced in artificial air. When test started, 0.35 g photocatalyst was put at the bottom of the chamber. Toluene standard gas was pumped into the chamber (about 450 mL) through PUMP1. The filled unit was kept in dark for 30 min to research the adsorption equilibrium between the photocatalyst and toluene.

An incident light source (a 300 W xenon lamp) was placed above the chamber which has a quartzose cover as an upper surface. At regular time intervals, the mixture gas in chamber was analyzed by gas chromatograph (7890A, Agilent, Santa Clara, CA, USA) connecting to the chamber. The constituent and the content of the mixture in the end of photocatalysis process were measured by gas chromatograph–mass spectrometry (GCMS-QP2010, Shimadzu, Osaka, Japan). The temperature of the unit was controlled using circulating cold water passing through the interlayer continuously to prevent thermal effect during the degradation process.

4. Conclusions

In summary, synthesized $Bi_2O_2CO_3$ nanosheets through hydrothermal method can be proven as a relative pure phase and no other composition is found when they were annealed in nitrogen at 150 °C. When annealed for various times at 150 °C, crystal facet of (002) of $Bi_2O_2CO_3$ has been exposed. The diffracted intensity ratio of (002)/(013) of BOC-150-8 h has been increased by 92%, which can help separate the photogenerated carries and improve the efficiency of removal toluene with removal rate up 99%. Moreover, CO_2 was verified to be the primary product in the photocatalytic degradation of toluene. As a result, the photocatalytic performance of $Bi_2O_2CO_3$ for removal toluene can be optimized through facile heat treatment. This work can probably be extended to applications of $Bi_2O_2CO_3$ in air purification.

Supplementary Materials: The following are available online at http://www.mdpi.com/2073-4344/10/4/389/s1, Figure S1: The photocatalysis equipment for photocatalystic removal of toluene in air; Figure S2: The colors of as-prepared samples annealed in nitrogen for four hours at different temperature after the irradiation of light; Figure S3: SEM images of BOC-150-12 h (a), BOC-150-24 h (b) and BOC-150-48 h (c); Figure S4: The colors of as-prepared samples annealed in nitrogen for various time at 150 °C after the irradiation of light; Figure S5: the total ion chromatograms (a) and the mass spectrum of CO_2 (b) and toluene (c) for BOC-150-4 h; Figure S6: the total lon chromatograms (a) and the mass spectrum of CO_2 (b) and toluene (c) for BOC-150-8 h; Figure S7: the total lon chromatograms (a) and the mass spectrum of CO_2 (b) for BOC-150-12 h; Figure S8: the total lon chromatograms (a) and the mass spectrum of CO_2 (b) and toluene (c) for BOC-150-24 h; Figure S9: the total lon chromatograms (a) and the mass spectrum of CO_2 (b) and toluene (c) for BOC-150-48 h; Table S1: N_2 physisorption results for different catalysts; Table S2: Results of BET surface areas and band gaps of $Bi_2O_2CO_3$ sample; Table S3: Rates and quantum fields of the photocatalytic CO_2 production using the as-prepared $Bi_2O_2CO_3$ samples.

Author Contributions: Investigation, J.D., H.W., Y.L. (Yidong Luo) and Y.X.; Methodology, J.D., H.W. and J.L.; Supervision, Y.L. (Yuanhua Lin); Writing and original draft, J.D.; Review & editing, Y.X. All authors have read and agreed to the published version of the manuscript.

Funding: This work was supported by the National Natural Science Foundation of China (Grant Nos. 51532002 and 51532003).

Conflicts of Interest: The authors declare no conflict of interest.

References

1. Gupta, S.; Khare, M.; Goyal, R. Sick building syndrome—A case study in a multistory centrally air-conditioned building in the Delhi City. *Build. Environ.* **2007**, *42*, 2797–2809. [CrossRef]

2. Jones, A.P. Indoor air quality and health. *Atmos. Environ.* **1999**, *33*, 4535–4564. [CrossRef]
3. Wolkoff, P. Trends in Europe to reduce the indoor air pollution of VOCs. *Indoor Air* **2003**, *13*, 5–11. [CrossRef]
4. Shin, S.-H.; Jo, W.-K. Longitudinal variations in indoor VOC concentrations after moving into new apartments and indoor source characterization. *Environ. Sci. Pollut. Res.* **2012**, *20*, 3696–3707. [CrossRef] [PubMed]
5. Qu, J.; Chen, D.; Li, N.; Xu, Q.; Li, H.; He, J.; Lu, J. Ternary photocatalyst of atomic-scale Pt coupled with MoS_2 co-loaded on TiO_2 surface for highly efficient degradation of gaseous toluene. *Appl. Catal. B Environ.* **2019**, *256*, 117877–117885. [CrossRef]
6. Liu, Z.; Chen, F.; Fang, P.; Wang, S.; Gao, Y.; Zheng, F.; Liu, Y.; Dai, Y. Study of adsorption-assisted photocatalytic oxidation of benzene with TiO_2/SiO_2 nanocomposites. *Appl. Catal. A* **2013**, *451*, 120–126. [CrossRef]
7. Chen, Y.; Cao, X.; Gao, B.; Lin, B. A facile approach to synthesize N-doped and oxygen-deficient TiO_2 with high visible-light activity for benzene decomposition. *Mater. Lett.* **2013**, *94*, 154–157. [CrossRef]
8. Pham, T.D.; Lee, B.K. Novel adsorption and photocatalytic oxidation for removal of gaseous toluene by V-doped TiO_2/PU under visible light. *J. Hazard. Mater.* **2015**, *300*, 493–503. [CrossRef]
9. Chen, Y.-C.; Katsumata, K.-I.; Chiu, Y.-H.; Okada, K.; Matsushita, N.; Hsu, Y.-J. ZnO-graphene composites as practical photocatalysts for gaseous acetaldehyde degradation and electrolytic water oxidation. *Appl. Catal. A Gen.* **2015**, *490*, 1–9. [CrossRef]
10. Katsumata, K.; Motoyoshi, R.; Matsushita, N.; Okada, K. Preparation of graphitic carbon nitride (g-C_3N_4)/WO_3 composites and enhanced visible-light-driven photodegradation of acetaldehyde gas. *J. Hazard. Mater.* **2013**, *260*, 475–482. [CrossRef]
11. Sugrañez, R.; Balbuena, J.; Yusta, M.C.; Martin, F.; Morales, J.; Sánchez, L. Efficient behaviour of hematite towards the photocatalytic degradation of NO gases. *Appl. Catal. B Environ.* **2015**, *165*, 529–536. [CrossRef]
12. Zhu, A.; Zhou, Y.; Wang, Y.; Zhu, Q.; Liu, H.; Zhang, Z.; Lu, H. Catalytic combustion of VOCs on Pt/CuMnCe and Pt/CeY honeycomb monolithic catalysts. *J. Rare Earths* **2018**, *36*, 1272–1277. [CrossRef]
13. Tang, W.; Wu, X.; Liu, G.; Li, S.; Li, D.; Li, W.; Chen, Y. Preparation of hierarchical layer-stacking Mn-Ce composite oxide for catalytic total oxidation of VOCs. *J. Rare Earths* **2015**, *33*, 62–69. [CrossRef]
14. Handa, M.; Lee, Y.; Shibusawa, M.; Tokumura, M.; Kawase, Y. Removal of VOCs in waste gas by the photo-Fenton reaction: Effects of dosage of Fenton reagents on degradation of toluene gas in a bubble column. *J. Chem. Technol. Biotechnol.* **2012**, *88*, 88–97. [CrossRef]
15. Ao, C.; Lee, S.-C.; Yu, J.Z.; Xu, J. Photodegradation of formaldehyde by photocatalyst TiO_2: Effects on the presences of NO, SO_2 and VOCs. *Appl. Catal. B Environ.* **2004**, *54*, 41–50. [CrossRef]
16. Assadi, A.A.; Bouzaza, A.; Merabet, S.; Wolbert, D. Modeling and simulation of VOCs removal by nonthermal plasma discharge with photocatalysis in a continuous reactor: Synergetic effect and mass transfer. *Chem. Eng. J.* **2014**, *258*, 119–127. [CrossRef]
17. Le Bechec, M.; Kinadjian, N.; Ollis, D.; Backov, R.; Lacombe, S.; Kinadjan, N. Comparison of kinetics of acetone, heptane and toluene photocatalytic mineralization over TiO_2 microfibers and Quartzel® mats. *Appl. Catal. B Environ.* **2015**, *179*, 78–87. [CrossRef]
18. Wang, Y.; Jiang, S.; Liu, F.; Zhao, C.; Zhao, D.; Li, X. Study on preparation and toluene removal of BiOI/Bi_2WO_6/ACF photocatalyst. *Appl. Surf. Sci.* **2019**, *488*, 161–169. [CrossRef]
19. Liu, H.; Chen, P.; Yuan, X.; Zhang, Y.; Huang, H.; Wang, L.; Dong, F. Pivotal roles of artificial oxygen vacancies in enhancing photocatalytic activity and selectivity on $Bi_2O_2CO_3$ nanosheets. *Chin. J. Catal.* **2019**, *40*, 620–630. [CrossRef]
20. Taylor, P.; Sunder, S.; Lopata, V.J. Structure, spectra, and stability of solid bismuth carbonates. *Can. J. Chem.* **1984**, *62*, 2863–2873. [CrossRef]
21. Chen, R.; So, M.H.; Yang, J.; Deng, F.; Che, C.-M.; Sun, H. Fabrication of bismuth subcarbonate nanotube arrays from bismuth citrate. *Chem. Commun.* **2006**, 2265. [CrossRef]
22. Zhang, Q.; Yuan, S.; Xu, B.; Xu, Y.; Cao, K.; Jin, Z.; Ohno, T. A facile approach to build $Bi_2O_2CO_3$/PCN nanohybridphotocatalysts for gaseous acetaldehyde efficient removal. *Catal. Today* **2018**, *315*, 184–193. [CrossRef]
23. Huang, H.; Li, X.; Wang, J.; Dong, F.; Chu, P.K.; Zhang, T.; Zhang, Y. Anionic Group Self-Doping as a Promising Strategy: Band-Gap Engineering and Multi-Functional Applications of High-Performance CO32-Doped $Bi_2O_2CO_3$. *ACS Catal.* **2015**, *5*, 4094–4103. [CrossRef]

24. Wang, F.; Zhao, Z.; Zhang, K.; Dong, F.; Zhou, Y. Topochemical transformation of low energy crystal facets to high energy facets: A case from $Bi_2O_2CO_3$ {001} facets to β-Bi_2O_3 {001} facets with improved photocatalytic oxidation of NO. *CrystEngComm* **2015**, *17*, 6098–6102. [CrossRef]
25. Huang, H.; Wang, J.; Dong, F.; Guo, Y.; Tian, N.; Zhang, Y.; Zhang, T. Highly Efficient $Bi_2O_2CO_3$Single-Crystal Lamellas with Dominantly Exposed {001} Facets. *Cryst. Growth Des.* **2015**, *15*, 534–537. [CrossRef]
26. Zheng, Y.; Duan, F.; Chen, M.; Xie, Y. Synthetic $Bi_2O_2CO_3$ nanostructures: Novel photocatalyst with controlled special surface exposed. *J. Mol. Catal. A Chem.* **2010**, *317*, 34–40. [CrossRef]
27. Zhao, Z.; Zhou, Y.; Wang, F.; Zhang, K.; Yu, S.; Cao, K. Polyaniline-decorated {001} facets of $Bi_2O_2CO_3$ nanosheets: In situ oxygen vacancy formation and enhanced visible light photocatalytic activity. *ACS Appl. Mater. Interfaces* **2015**, *7*, 730–737. [CrossRef]
28. Lu, Y.; Huang, Y.; Zhang, Y.; Huang, T.; Li, H.; Cao, J.-J.; Ho, W. Effects of H2O2 generation over visible light-responsive Bi/Bi_2O_2−CO_3 nanosheets on their photocatalytic NO removal performance. *Chem. Eng. J.* **2019**, *363*, 374–382. [CrossRef]
29. Wang, Z.; Huang, Y.; Chen, L.; Chen, M.; Cao, J.; Ho, W.; Lee, S.C. In situ g-C_3N_4 self-sacrificial synthesis of a g-C_3N_4/$LaCO_3OH$ heterostructure with strong interfacial charge transfer and separation for photocatalytic NO removal. *J. Mater. Chem. A* **2018**, *6*, 972–981. [CrossRef]
30. Yang, C.; Xue, Z.; Qin, J.; Sawangphruk, M.; Rajendran, S.; Zhang, X.; Liu, R. Visible Light-Driven Photocatalytic H-2 Generation and Mechanism Insights into $Bi_2O_2CO_3$/G-C_3N_4 Z-Scheme Photocatalyst. *J. Phys. Chem. C* **2019**, *123*, 4795–4804. [CrossRef]
31. Xu, R.; Su, M.; Liu, Y.; Chen, Z.; Ji, C.; Yang, M.; Chang, X.; Chen, D. Comparative study on the removal of different-type organic pollutants on hierarchical tetragonal bismutite microspheres: Adsorption, degradation and mechanism. *J. Clean. Prod.* **2020**, *242*, 118366. [CrossRef]
32. Weon, S.; He, F.; Choi, W. Status and challenges in photocatalytic nanotechnology for cleaning air polluted with volatile organic compounds: Visible light utilization and catalyst deactivation. *Environ. Sci. Nano* **2019**, *6*, 3185–3214. [CrossRef]
33. Liu, Y.; Wang, Z.; Huang, B.; Yang, K.; Zhang, X.; Qin, X.; Dai, Y. Preparation, electronic structure, and photocatalytic properties of $Bi_2O_2CO_3$ nanosheet. *Appl. Surf. Sci.* **2010**, *257*, 172–175. [CrossRef]
34. Chen, L.; Huang, R.; Yin, S.; Luo, S.-L.; Au, C.T. Flower-like $Bi_2O_2CO_3$: Facile synthesis and their photocatalytic application in treatment of dye-containing wastewater. *Chem. Eng. J.* **2012**, *193*, 123–130. [CrossRef]
35. Dong, F.; Lee, S.C.; Wu, Z.; Huang, Y.; Fu, M.; Ho, W.K.; Zou, S.; Wang, B. Rose-Like Monodisperse Bismuth SubcarbonateHierarchical Hollow Microspheres: One-pot Template-Free Fabricationand Excellent Visible Light Photocatalytic Activity and PhotochemicalStability for NO Removal in Indoor Air. *J. Hazard. Mater.* **2011**, *195*, 346–354. [CrossRef]
36. Zhou, Y.; Wang, H.; Sheng, M.; Zhang, Q.; Zhao, Z.; Lin, Y.; Liu, H.; Patzke, G.R. Environmentally friendly room temperature synthesis and humidity sensing applications of nanostructured $Bi_2O_2CO_3$. *Sens. Actuators B Chem.* **2013**, *188*, 1312–1318. [CrossRef]
37. Lu, Y.; Huang, Y.; Zhang, Y.; Cao, J.J.; Li, H.; Bian, C.; Lee, S.C. Oxygen vacancy engineering of Bi_2O_3/$Bi_2O_2CO_3$ heterojunctions Implications of the interfacial charge transfer, NO adsorption and removal. *Appl. Catal. B Environ.* **2018**, *231*, 357–367. [CrossRef]
38. Jiang, J.; Zhang, L.; Li, H.; He, W.; Yin, J.-J. Self-doping and surface plasmon modification induced visible light photocatalysis of BiOCl. *Nanoscale* **2013**, *5*, 10573. [CrossRef]
39. Fan, W.; Li, H.; Zhao, F.; Xiao, X.; Huang, Y.; Ji, H.; Tong, Y. Boosting the photocatalytic performance of (001) BiOI: Enhancing donor density and separation efficiency of photogenerated electrons and holes. *Chem. Commun.* **2016**, *52*, 5316–5319. [CrossRef]
40. Wang, C.; Shao, C.; Liu, Y.; Zhang, L. Photocatalytic properties BiOCl and Bi_2O_3 nanofibers prepared by electrospinning. *Scr. Mater.* **2008**, *59*, 332–335. [CrossRef]
41. Houc, W.; Hu, T.; Du, N.; Zhang, R.; Liu, J.-Q.; Hou, W. Wavelength-dependent differences in photocatalytic performance between BiOBrnanosheets with dominant exposed (0 0 1) and (0 1 0) facets. *Appl. Catal. B Environ.* **2016**, *187*, 342–349.
42. Ding, J.; Wang, H.; Xu, H.; Qiao, L.; Luo, Y.; Lin, Y.; Nan, C. Synthesis and Broadband Spectra Photocatalytic Properties of $Bi_2O_2(CO_3)_{1-x}Sx$. *Materials* **2018**, *11*, 791. [CrossRef] [PubMed]
43. Bai, P.; Tong, X.; Wan, J.; Gao, Y.; Xue, S. Flower-like $Bi_2O_2CO_3$-mediated selective oxidative coupling processes of amines under visible light irradiation. *J. Catal.* **2019**, *374*, 257–265. [CrossRef]

44. Nethercot, A.H. Prediction of Fermi Energies and Photoelectric Thresholds Based on Electronegativity Concepts. *Phys. Rev. Lett.* **1974**, *33*, 1088–1091. [CrossRef]
45. Dong, F.; Zheng, A.; Sun, Y.; Fu, M.; Jiang, B.; Ho, W.-K.; Lee, S.-C.; Wu, Z. One-pot template-free synthesis, growth mechanism and enhanced photocatalytic activity of monodisperse $(BiO)_2CO_3$ hierarchical hollow microspheres self-assembled with single-crystalline nanosheets. *CrystEngComm* **2012**, *14*, 3534. [CrossRef]
46. Cao, J.; Li, X.; Lin, H.; Chen, S.; Fu, X. In stiu preparation of novel p-n junctionphotocatalystBiOI/$(BiO)_2CO_3$ with enhanced visible light photocatalyticactivity. *J. Hazard. Mater.* **2012**, *239–240*, 316–324. [CrossRef]
47. Peng, S.; Li, L.; Tan, H.; Wu, Y.; Cai, R.; Yu, H.; Huang, X.; Zhu, P.; Ramakrishna, S.; Srinivasan, M.; et al. Monodispersed Ag nanoparticles loaded on the PVP-assisted synthetic $Bi_2O_2CO_3$ microspheres with enhanced photocatalyticandsupercapacitive performances. *J. Mater. Chem. A* **2013**, *1*, 7630–7638. [CrossRef]
48. D'Hennezel, O.; Pichat, P.; Ollis, D.F. Benzene and toluene gas-phase photocatalytic degradation over H_2O and HCL pretreated TiO_2: By-products and mechanisms. *J. Photochem. Photobiol. A Chem.* **1998**, *118*, 197–204. [CrossRef]